



Article

# 3D MRI Reconstruction Based on 2D Generative Adversarial Network Super-Resolution

Hongtao Zhang <sup>1,\*</sup> , Yuki Shinomiya <sup>2</sup>  and Shinichi Yoshida <sup>2</sup><sup>1</sup> Graduate School of Engineering, Kochi University of Technology, Kami, Kochi 782-8502, Japan<sup>2</sup> School of Information, Kochi University of Technology, Kami, Kochi 782-8502, Japan; shinomiya.yuki@kochi-tech.ac.jp (Y.S.); yoshida.shinichi@kochi-tech.ac.jp (S.Y.)

\* Correspondence: 237001c@gs.kochi-tech.ac.jp; Tel.: +81-887-53-1111

**Abstract:** The diagnosis of brain pathologies usually involves imaging to analyze the condition of the brain. Magnetic resonance imaging (MRI) technology is widely used in brain disorder diagnosis. The image quality of MRI depends on the magnetostatic field strength and scanning time. Scanners with lower field strengths have the disadvantages of a low resolution and high imaging cost, and scanning takes a long time. The traditional super-resolution reconstruction method based on MRI generally states an optimization problem in terms of prior information. It solves the problem using an iterative approach with a large time cost. Many methods based on deep learning have emerged to replace traditional methods. MRI super-resolution technology based on deep learning can effectively improve MRI resolution through a three-dimensional convolutional neural network; however, the training costs are relatively high. In this paper, we propose the use of two-dimensional super-resolution technology for the super-resolution reconstruction of MRI images. In the first reconstruction, we choose a scale factor of 2 and simulate half the volume of MRI slices as input. We utilize a receiving field block enhanced super-resolution generative adversarial network (RFB-ESRGAN), which is superior to other super-resolution technologies in terms of texture and frequency information. We then rebuild the super-resolution reconstructed slices in the MRI. In the second reconstruction, the image after the first reconstruction is composed of only half of the slices, and there are still missing values. In our previous work, we adopted the traditional interpolation method, and there was still a gap in the visual effect of the reconstructed images. Therefore, we propose a noise-based super-resolution network (nESRGAN). The noise addition to the network can provide additional texture restoration possibilities. We use nESRGAN to further restore MRI resolution and high-frequency information. Finally, we achieve the 3D reconstruction of brain MRI images through two super-resolution reconstructions. Our proposed method is superior to 3D super-resolution technology based on deep learning in terms of perception range and image quality evaluation standards.

**Keywords:** magnetic resonance imaging; deep learning; super-resolution; three-dimensional reconstruction; RFB-ESRGAN; nESRGAN



**Citation:** Zhang, H.; Shinomiya, Y.; Yoshida, S. 3D MRI Reconstruction Based on 2D Generative Adversarial Network Super-Resolution. *Sensors* **2021**, *21*, 2978. <https://doi.org/10.3390/s21092978>

Academic Editors: Hossam A. Gabbar and Paola Saccomandi

Received: 31 January 2021

Accepted: 20 April 2021

Published: 23 April 2021

**Publisher's Note:** MDPI stays neutral with regard to jurisdictional claims in published maps and institutional affiliations.



**Copyright:** © 2021 by the authors. Licensee MDPI, Basel, Switzerland. This article is an open access article distributed under the terms and conditions of the Creative Commons Attribution (CC BY) license (<https://creativecommons.org/licenses/by/4.0/>).

## 1. Introduction

The diagnosis of brain lesions is an active field of research. Magnetic resonance imaging (MRI) is one of the most important diagnostic imaging methods and has been widely used in diagnosis and image-guided treatment, especially for brain imaging diagnosis. Through brain MRI, brain abnormalities and lesions can be observed. MRI scanners with higher magnetic field strength provide higher signal-to-noise ratio (SNR) [1–4]. At present, the 1.5 T MRI scanner is a commonly used instrument in hospitals. Compared with a 3 T MRI scanner, the time cost of image acquisition using a 1.5 T MRI scanner is higher because its SNR is lower. Due to imaging technology limitations, such as high SNR and long scanning time, image super-resolution (SR) is favored by medical experts [5].

Early research on super-resolution MRI images used super-resolution reconstruction (SRR) to improve the image resolution. SRR combines a series of low-resolution MRI

images into a high-resolution image [5–7]. This method requires large time and equipment costs, and subsequent research has shown that adding more low-resolution scans does not necessarily improve the resolution [8,9]. Subsequently, with the introduction of single-image super-resolution (SISR) [10,11], MRI super-resolution reconstruction only requires low-resolution scans corresponding to high-resolution output. Initially, SISR used a form of regularization conditions and then used prior knowledge to enhance the reconstruction ability of linear models [11]. However, this type of method is computationally complex and requires many computing resources [5,7,12].

Based on the convolutional neural network (CNN) model, the super-resolution CNN (SRCNN) [13] was introduced into SISR. MRI super-resolution research attempted to combine convolutional neural networks for super-resolution reconstruction [5,7–9]. With the introduction of residual networks [14–19], super-resolution technology based on deep learning began to develop into deeper networks [14–16]. However, the reconstructed images are usually too smooth and lack visual authenticity, depending on the mean square error (MSE) loss function. With the introduction of generative adversarial networks (GANs) [20], the blurring image problem is improved, and SISR has been developed to reduce perceived loss [19]. MRI super-resolution reconstruction is focused on GANs to restore more textural details and high-frequency information rather than overall clarity.

We consider that MRI is stored in a three-dimensional matrix. MRI super-resolution reconstruction is usually combined with a three-dimensional convolutional neural network (3D-CNN), which can directly extract 3D image features to reconstruct the entire MRI image. However, it can be computationally complex and cause memory allocation problems. Therefore, we propose using 2D CNNs to replace 3D CNNs in order to reduce memory and time costs. Combined with a scale factor of 2, the entire MRI data reconstruction should be a half-volume MRI (Figure 1, 2D in Figure 2), so we preprocessed half number of the MRI slices as a dataset in the slice processing. We rebuilt the reconstructed slices in the three planes into an MRI image to complete the first reconstruction step (Figure 1). Because MRI involves reconstructing half the number of slices in three planes, there are missing values in the reconstructed MRI. Therefore, we propose the second super-resolution reconstruction work for detail restoration. After two super-resolution reconstructions, we realized three-dimensional MRI reconstruction in the two-dimensional super-resolution convolutional neural network.

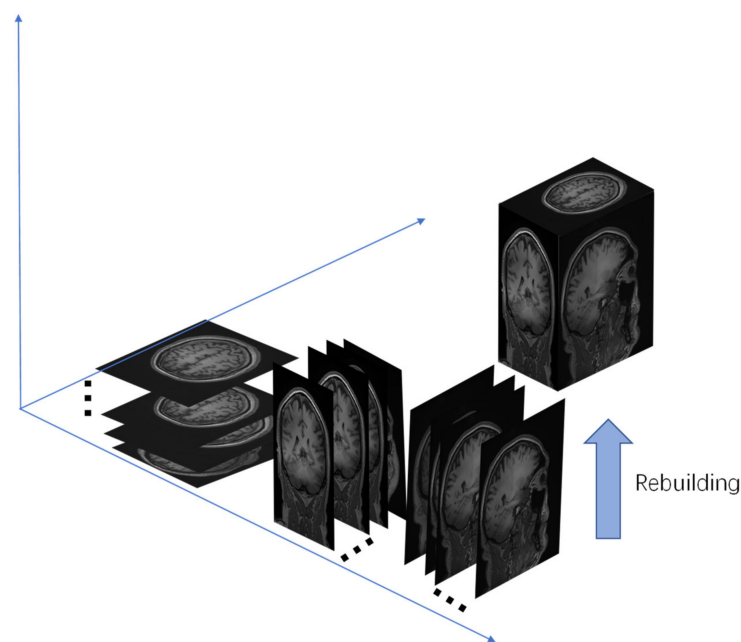


**Figure 1.** Rebuilding MRI from three plane slices. Number of slices is half that of MRI. Number of slices in three directions is 128 ( $256 \times 150$  pixels), 128 ( $256 \times 150$  pixels), and 75 ( $256 \times 256$  pixels).

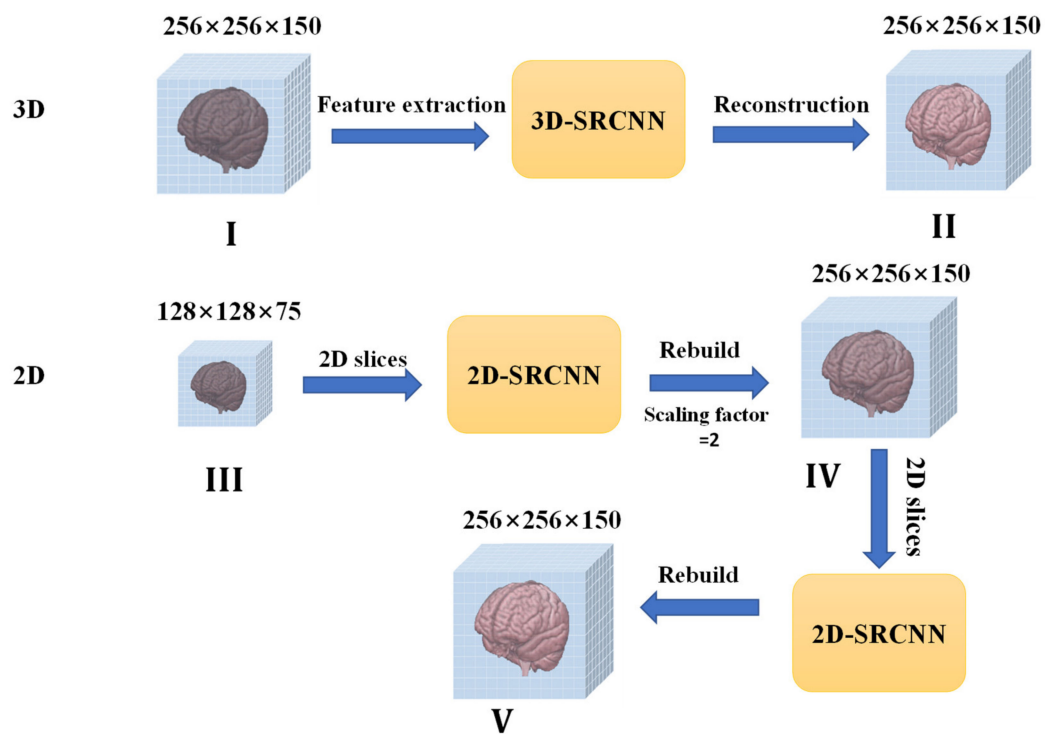


**Figure 2.** Main processes of proposed method. I and II: MRI super-resolution reconstruction for three-dimensional convolutional neural network (3D-CNN). Our method includes III, IV, and V. Depending on scaling factor, input shape is half of MRI ( $128 \times 128 \times 75$ ), which consists of 128 ( $128 \times 75$ ), 128 ( $128 \times 75$ ), and 75 ( $128 \times 128$ ) slices. In process IV, through two-dimensional super-resolution CNN (2D-SRCNN), MRI can be recovered with more detail and rebuilding can be finished.

The main contributions of this paper include the following:

- (1) A new noise-based enhanced super-resolution generative adversarial network (nESR-GAN) with the addition of noise and interpolated sampling is proposed. The noise part of the network can provide specific high-frequency information and details without affecting the overall feature recovery. Simultaneously, interpolation sampling solves artifacts and color changes caused by the checkerboard effect [21].
- (2) Our proposed method is better than the super-resolution method based on 3D neural networks in respect of the reconstruction effect. The high-resolution MRI images can assist doctors in obtaining more detailed brain information, which is of particular significance for diagnosing and predicting brain diseases by using a 1.5 T MRI scanner.

The related methods are outlined in Section 2. Section 3 introduces the relevant configuration and parameters of the study. In Section 4, we present the results and analysis. In Section 5, we discuss the experimental data and results, summarize the experiment, and describe the main work planned for the future.

## 2. Main Method of Reconstruction

### 2.1. Main Idea and Processes

In most super-resolution studies of MRI, researchers often use three-dimensional convolutional neural networks for image reconstruction [22–24]. However, the three-dimensional convolutional neural networks has excessive parameters and large weight, which results in a considerable memory cost. An MRI image is usually saved in the form of a voxel matrix. According to the matrix's particularity, MRI rebuilding can be completed with half the number of slices in three directions, but there are many missing values (as shown in Figure 1). In 3D-SRCNN, MRI structure information is generally read to perform reconstruction (as shown in the 3D-SRCNN in Figure 2). Using a two-dimensional CNN to replace a three-dimensional CNN can reduce computational costs. As shown in Figure 2,

our study's scaling factor is 2, and thereby we simulate half of volume MRI as the dataset. Compared with whole MRI data, it only includes a half number of slices in three planes. We adopted the MRI slice operation. After reconstruction from 2D-SRCNN, new MRI data is rebuilt by these reconstructed slices (Figure 1). Since the reconstructed MRI only contains half the number of slices, there have been missing values. For the problem of missing values, we can use the new 2D-SRCNN network for further recovery. In the second step of recovery work, we utilize the same slicing operation in new 2D-SRCNN and obtain a new MRI consisting of newly reconstructed slices. After the first and second steps, we succeeded in replacing the 3D-SRCNN and completed the super-resolution reconstruction of the MRI. In general, we propose two neural networks to perform reconstruction work. The first reconstruction work is based on the structural particularity of the MRI voxel matrix. Half the number of slices (half the volume) are selected for super-resolution reconstruction and MRI rebuilding. The second reconstruction work uses super-resolution technology to further repair the missing values of the reconstructed MRI to complete the rebuilding.

In deep learning, MRI super-resolution reconstruction technology is based on learning high-resolution image features from a great deal of MRI data [25,26]. In recent years, the use of generated adversarial neural networks (GANs) for super-resolution reconstruction has become the mainstream [25]. With GANs, restored images have more detailed features. Among many super-resolution adversarial neural networks, ESRGAN with a receptive field module is superior to other methods in restoring high-frequency details and maintaining content consistency. Receiving field block (RFB)-ESRGAN [19] can obtain more detailed information for brain MRI (Table 1). Therefore, we adopted RFB-ESRGAN in the first reconstruction work. Taking into account the interactivity of MRI in three planes, each slice in the rebuilt MRI image has missing values due to insufficient pixel information.

In the experimental part of our study, the primary process of 3D reconstruction is to perform two super-resolution reconstructions. In the first reconstruction, we use an expansion parameter whose size is 2. Therefore, the entire MRI involved in training should also be half the volume. After performing super-resolution reconstruction on low-resolution two-dimensional slices, rebuilding is performed. The reconstituted MRI image has only a half number of the slices in all three planes. Considering the interactivity, each slice in this new image has missing values. In our previous work, we referred to linear interpolation and used surrounding non-zero pixels in the zero value of each slice and then performed substitution and interpolation in the second reconstruction. However, we found that there were differences in brightness between the reconstituted brain MRI slices. At the same time, traditional interpolation repair can only solve the issue of brightness. There are still noise and missing values in the interpolated slices (as shown in Figure 3), so we propose a noise-based network (nESRGAN) to perform the second super-resolution reconstruction. Inspired by Style-GAN [28], we found that the addition of noise can help in restoring features and supplementing more high-frequency information. Similarly, ESRGAN also causes the checkerboard effect as a result of deconvolution [21]. Therefore, we propose an interpolation sampling recovery block to replace the deconvolution layer so that the reconstructed image no longer has a checkerboard pattern of different colors.

**Table 1.** Comparison of super-resolution methods on CNN/GAN with 2D MRI images (average  $\pm$  standard deviation). Our approach achieves best performance in three planes. Red font indicates best performance, blue font indicates second best performance. PSNR, peak signal-to-noise ratio; LPIPS, learned perceptual image patch similarity. FSRCNN [27] is enhanced method based on SRCNN, and EDSR is first method of using deep residual network [15].

Plane/ Method	Evaluation	LR	CNN		Deep Network	GAN		
		Bicubic	SRCNN	FSRCNN	EDSR	SRGAN	ESRGAN	RFB-ESRGAN
Sagittal	PSNR $\uparrow$	25.13	14.40 $\pm$ 0.22	25.77 $\pm$ 0.56	25.62 $\pm$ 0.31	26.45 $\pm$ 0.64	25.37 $\pm$ 0.45	26.20 $\pm$ 0.59
	SSIM $\uparrow$	0.8106	0.3196 $\pm$ 0.0095	0.8337 $\pm$ 0.0041	0.8963 $\pm$ 0.0035	0.8959 $\pm$ 0.0057	0.8856 $\pm$ 0.0054	0.9201 $\pm$ 0.0041
	LPIPS $\downarrow$	0.1996	0.3228 $\pm$ 0.0127	0.2140 $\pm$ 0.0044	0.1501 $\pm$ 0.0043	0.1522 $\pm$ 0.0064	0.1525 $\pm$ 0.0054	0.1411 $\pm$ 0.0043
Coronal	PSNR $\uparrow$	26.95	14.10 $\pm$ 0.37	29.25 $\pm$ 0.64	27.70 $\pm$ 0.80	29.16 $\pm$ 0.79	29.15 $\pm$ 0.86	29.94 $\pm$ 0.83
	SSIM $\uparrow$	0.7491	0.4175 $\pm$ 0.0516	0.7732 $\pm$ 0.0124	0.9430 $\pm$ 0.0047	0.9372 $\pm$ 0.0067	0.9366 $\pm$ 0.0049	0.9641 $\pm$ 0.0032
	LPIPS $\downarrow$	0.149	0.2411 $\pm$ 0.0127	0.1884 $\pm$ 0.0095	0.1006 $\pm$ 0.0087	0.1077 $\pm$ 0.0064	0.0807 $\pm$ 0.0092	0.0750 $\pm$ 0.0075
Axial	PSNR $\uparrow$	29.19	16.46 $\pm$ 0.44	28.42 $\pm$ 1.12	28.85 $\pm$ 1.09	27.69 $\pm$ 0.92	27.12 $\pm$ 0.88	30.69 $\pm$ 0.83
	SSIM $\uparrow$	0.8115	0.3682 $\pm$ 0.0301	0.8224 $\pm$ 0.0452	0.9417 $\pm$ 0.0056	0.9027 $\pm$ 0.0157	0.9083 $\pm$ 0.0089	0.9600 $\pm$ 0.0031
	LPIPS $\downarrow$	0.131	0.2519 $\pm$ 0.0120	0.2035 $\pm$ 0.0174	0.1005 $\pm$ 0.0088	0.1148 $\pm$ 0.0088	0.1104 $\pm$ 0.0079	0.0839 $\pm$ 0.0074

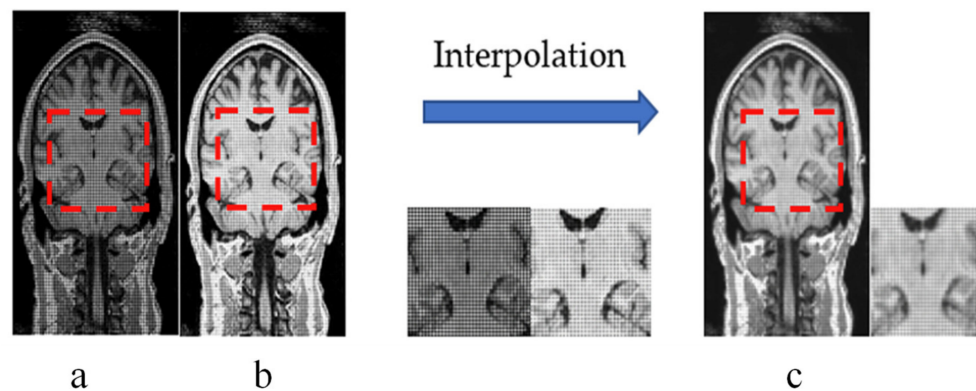


**Figure 3.** (a,b) Adjacent slices which are from with different brightness; Slices belong to the newly reconstructed MRI in the first reconstruction. (c) New slice after interpolation repair. Noise and grid lines still exist from traditional interpolation. Interpolation only solves the problem of brightness and recovers only a few details.

We use RFB-ESRGAN [19] for the first MRI reconstruction. After that, half a number of the MRI slices are reorganized to obtain an image with much noise and many missing values. Then we use nESRGAN to perform the super-resolution reconstruction, and finally rebuild a new high-resolution MRI image. The main processes are shown in Figure 4.

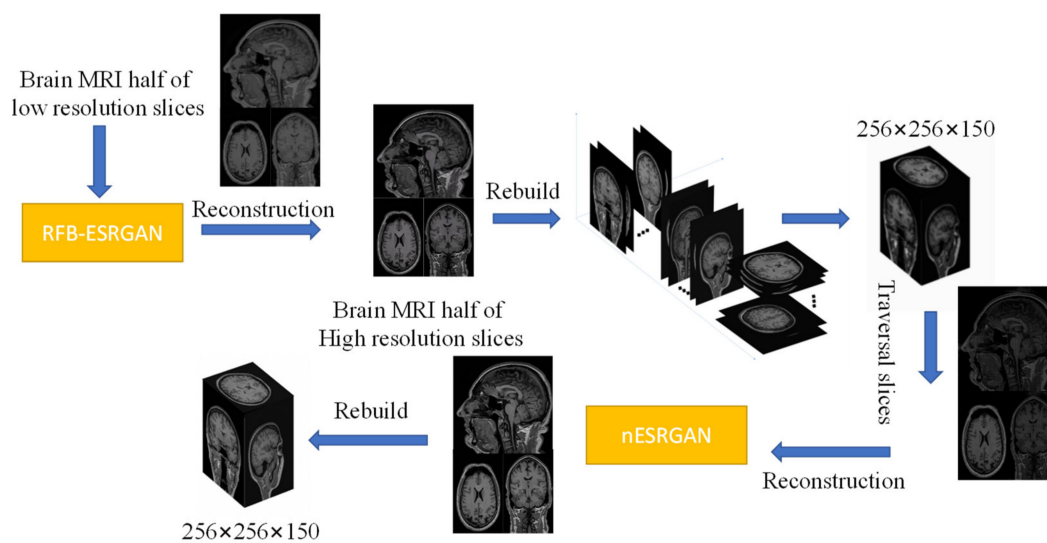


**Figure 4.** Main processes of experiment. Prepare slices on three planes (with an interval of 1 slice) for super-resolution reconstruction. Obtain high-resolution MRI slices through receiving field block enhanced super-resolution generative adversarial network (RFB-ESRGAN). Since there is half the number of slices, they can still be rebuilt into the MRI. Rebuilt MRI image has many missing values because half the slices are missing; then, super-resolution reconstruction is used to repair the image. Finally, super-resolution reconstruction is completed.

## 2.2. MRI Slice Reconstruction Based on RFB-ESRGAN

To obtain more MRI details and reduce network complexity, we propose RFB-ESRGAN for the first MRI super-resolution reconstruction. The main structure of the network is shown in Figure 5.

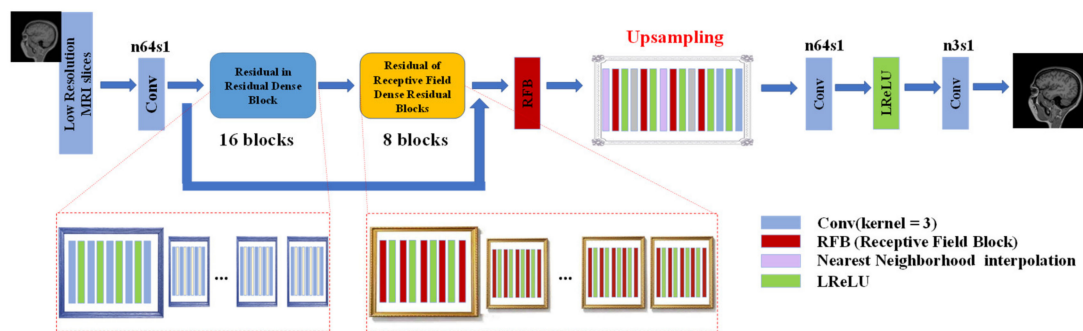


**Figure 5.** Generator network with  $k = 3$  kernel size,  $n = (3, 64, 256)$  feature maps, and  $s = 1$  stride. Network has 2 residual dense blocks, RRDB has 16 blocks, and RRFB has 8 blocks in the whole network. LReLU is activation function.

RFB-ESRGAN alternately uses the upsampling operations of nearest neighborhood interpolation (NNI) and sub-pixel convolution (SPC) to achieve a good blend of spatial and depth information that will not lose detail performance due to over-resolution. Alternating different upsampling methods reduces the computational complexity. To a certain extent, the super-resolution of multi-scale MRI images can be achieved.

In terms of generators, the network mainly includes the residuals in the dense residual blocks and the receptive field blocks. The residual receptive field block uses small convolution kernels of different sizes for detail restoration, reducing the number of model parameters and computational complexity. The network introduces receptive field blocks (RFBs) [19,29] to super-resolution, which balances the problems of small calculation and large receptive field, and can extract very detailed features, thereby obtaining more detailed textures of the MRI image. The network structure of the residual receptive field block is shown in Figure 6.

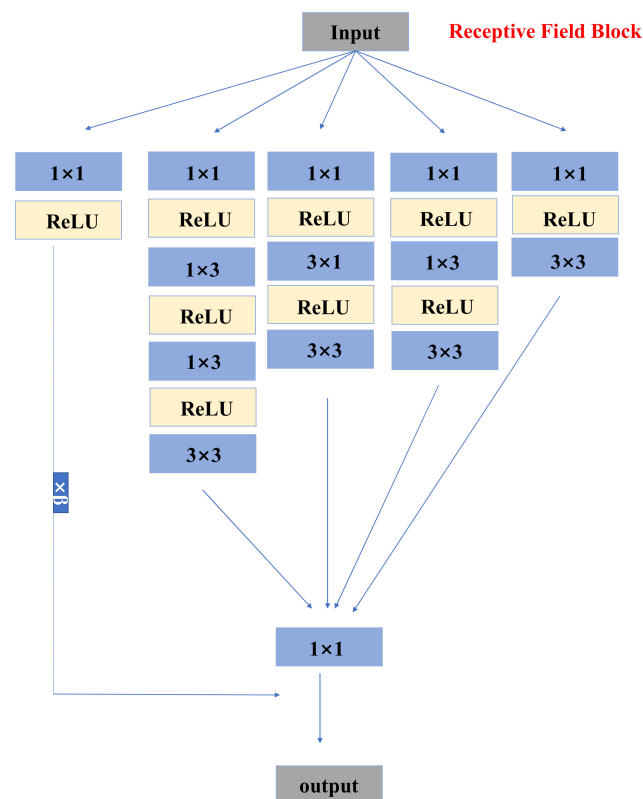


**Figure 6.** Structure of receptive field block (RFB). Block includes numerous small size kernels. RFB can provide detailed information. ReLU is activation function in network.

In terms of the discriminator, the network still uses the idea of Ra-GAN [30] to calculate the more realistic probability of the reconstructed MRI. The main structure is shown in Figure 7.

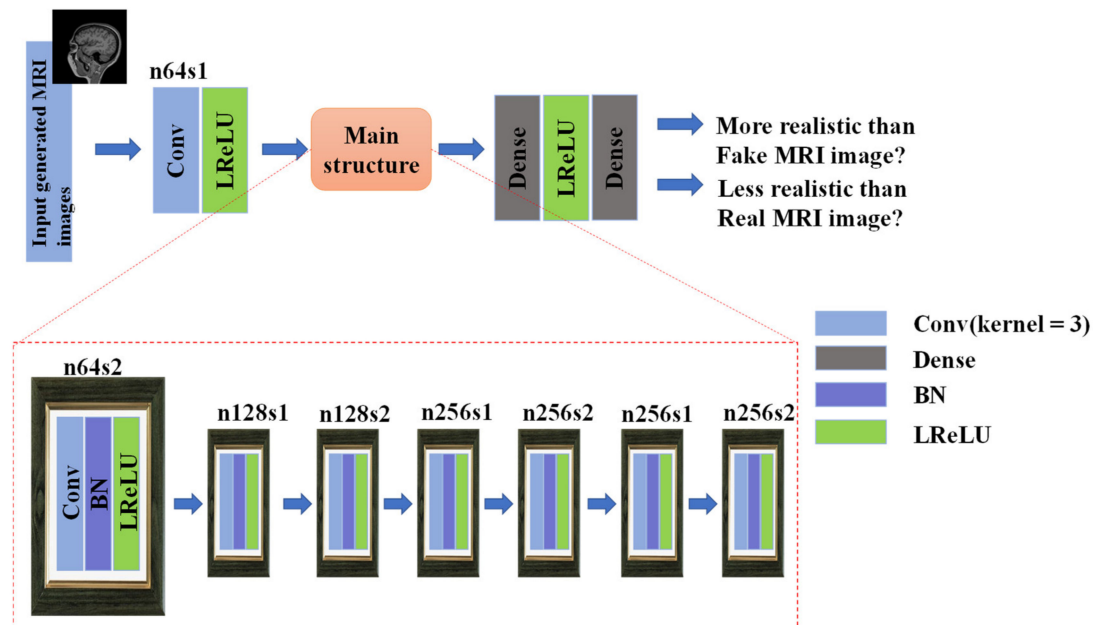


**Figure 7.** Discriminator network with  $k = 3$  kernel size,  $n = (64, 128, 256, 512)$  feature maps, and  $s = (1, 2)$  stride. In this network, dense is fully connected layer, BN is Batch Normalization and LReLU is activation function.

After setting up the network, we adopted two-stage training. The first stage uses L1 loss for training, then uses the second stage to introduce content loss and adversarial loss to fine-tune the model to avoid instability in the training process. Through the trained RFB-ESRGAN, we reconstructed half of the MRI images in three directions in each MRI. Then we used these MRI images to reconstruct a new MRI (first step in Figure 4).

### 2.3. MRI Slice Reconstruction Based on nESRGAN

To recover detailed information, we used nESRGAN for the second MRI reconstruction. The specific structure of the network is shown in Figure 8.

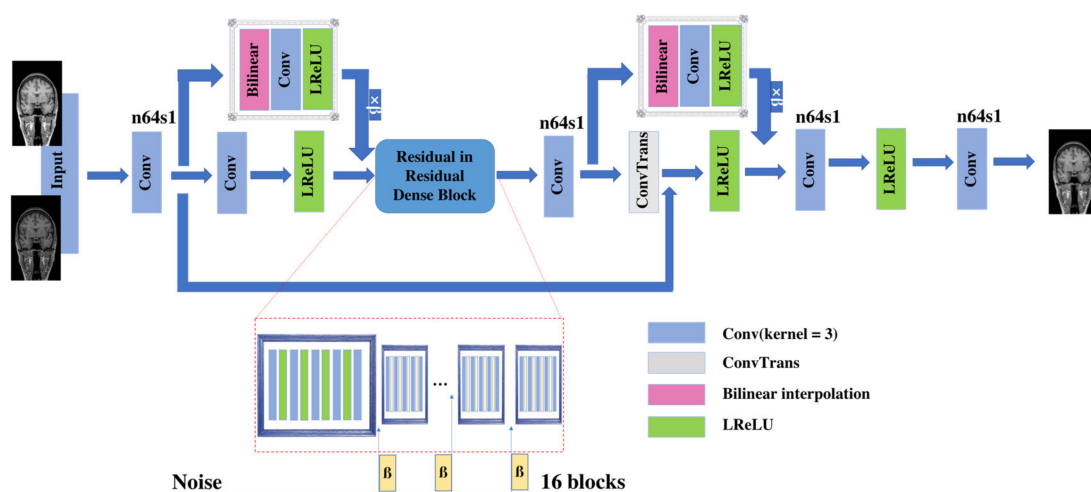


**Figure 8.** Generator network with  $k = 3$  kernel size,  $n = (3, 64)$  feature maps, and  $s = 1$  stride. Network has 16 residuals in residual dense blocks. ConvTrans is deconvolution layer. LReLU is activation function.



nESRGAN uses ESRGAN as the leading architecture. Aiming at the missing values in MRI, we added noise to the residuals in the residual dense block to generate certain detailed image information. At the same time, in order to avoid the checkerboard effect, we added interpolation sampling. The sampling block replaces the original deconvolution layer [21] to avoid artifacts. The slice does not need to be degraded, so when the scaling factor exists, we can add the sampling block in the feature extraction link to achieve down-sampling and obtain sufficient feature information. The discriminator network is consistent with RFB-ESRGAN (Figure 7).

In the training of nESRGAN, our dataset is sliced from the reconstructed MRI. The network includes a downsampling module, so there is no need for image degradation processing. We only need to traverse all MRI slices and then reconstruct a new image through the trained nESRGAN (the second step in Figure 4).

#### 2.4. Related Loss Function

The network loss used in our methods is consistent with ESRGAN. The generator loss part is composed of perceptual loss, adversarial loss, and pixel loss. The perceptual loss uses the VGG-19 [31] before activation as the extraction feature. The adversarial loss is the value of loss against the Ra-GAN [30] discriminator, and the pixel loss is the  $L1$  of the supervised learning enhancement output and the label [18,19,32]. The generator loss ( $L_G$ ) can be expressed as follows:

$$L_G = L_{\text{percep}} + \lambda L_G^{Ra} + \eta l_1 \quad (1)$$

$$L_{\text{percep}} = \sum ||\text{VGG}(I^{SR}) - \text{VGG}(I^{HR})||_1 \quad (2)$$

$L_{\text{percep}}$  is perceptual loss, which includes VGG adversarial loss ( $\text{VGG}(I^{SR}, I^{HR})$ ).  $\lambda$  and  $\eta$  are the coefficients to balance different loss terms.  $L_G^{Ra}$  reflects the probability that real images are relatively more realistic than fake images.  $l_1$  is pixel loss.  $L_G^{Ra}$  can be expressed as follows:

$$I^{SR} = G(I^{LR}) \quad (3)$$

$$L_G^{Ra} = \sum ||I^{SR} - I^{HR}||_1 \quad (4)$$

The loss of pixels is as follows:

$$l_1 = -E[\log(1 - \Delta_{Real})] - E[\log(\Delta_{Fake})] \quad (5)$$

$$\Delta_{Real} = \text{sigmoid}(D(I^{HR}) - E[D(I^{SR})]) \quad (6)$$

$$\Delta_{Fake} = \text{sigmoid}(D(I^{SR}) - E[D(I^{HR})]) \quad (7)$$

In terms of the discriminator, the idea of Ra-GAN is adopted. It mainly determines whether a picture is more real than another picture; that is, the real image is relatively more realistic than the fake image. The loss function is expressed as follows:

$$L_D^{RaSGAN} = -E_{x_r \sim P}[\log(\underline{D}(x_r))] - E_{x_f \sim Q}[\log(1 - \underline{D}(x_f))] \quad (8)$$

$$x = \text{sigmoid}(C(x) - E_{x_f \sim Q}C(x_f)) \text{ if } x \text{ is real}$$

$$x = \text{sigmoid}(C(x) - E_{x_r \sim P}C(x_r)) \text{ if } x \text{ is fake} \quad (9)$$

$P$  is the distribution of real data.  $Q$  is the distribution of fake data.  $x_f$  is the image generated by the generator, and  $x_r$  is the original image.  $C(x)$  and  $\underline{D}(x)$  are, respectively, defined as the output of the non-transform discriminator and the standard discriminator.

### 2.5. Image Quality Evaluation Indicators

Traditional MRI super-resolution reconstruction techniques generally follow the MSE-based peak signal-to-noise ratio (PSNR) [33] as the reconstructed image quality index. However, PSNR is based on error-sensitive image quality evaluation, in which the visual characteristics of the human eye are not considered. As a result, the evaluation results are often inconsistent with people's subjective feelings. As a result, images are too smooth and lack high-frequency information. For this reason, we added structural similarity (SSIM) [33] and learned perceptual image patch similarity (LPIPS) [34] as the evaluation criteria for reconstructed images. The higher the values of PSNR and SSIM, the lower the distortion of the picture. LPIPS [34] is used to evaluate the distance between image patches; the lower the value of LPIPS, the more similar the images.

PSNR and SSIM [33] can be expressed as follows:

$$PSNR = 10 \times \log_{10} \left( \frac{MAX_I^2}{MSE} \right) \quad (10)$$

$$SSIM(x, y) = \frac{(2\mu_x\mu_y + c_1)(2\sigma_{xy} + c_2)}{(\mu_x^2 + \mu_y^2 + c_1)(\sigma_x^2 + \sigma_y^2 + c_2)} \quad (11)$$

where  $\mu_x$  and  $\mu_y$  represent the mean values of images X and Y,  $\sigma_x$  and  $\sigma_y$  represent the variances of images X and Y, and  $\sigma_{xy}$  represents the covariances of images X and Y.

## 3. Comparisons and Configuration

### 3.1. Experimental Configuration

#### 3.1.1. Dataset

All MRI data comes from the IXI (Information eXtraction from Images) dataset, which includes structural MRI of 581 healthy adults. In this study, we use T1-weighted structural images. The dataset is freely available from the following website: <http://brain-development.org/ixi-dataset/> (accessed on 20 August 2020).

This study uses T1 brain MRI data, with a primary size of  $256 \times 256 \times 150$  pixels, and the main data format is NIfTI. A total of 581 pieces of T1-weighted brain data were used; We divided the dataset according to the ratio of 7:3. 431 pieces of data as the training set, and the remaining 150 as the test set. In preparing the dataset at the beginning of the experiment, we performed degradation processing of low-resolution images through the bicubic difference. The size of slices on the three planes was half the original size. We divided each slice into multiple image patches. The sizes of the paired LR and HR images were  $16 \times 16$  and  $32 \times 32$ , respectively.

In the first reconstruction of this research, we adopted sampling slices with an interval of 1 slice and obtained half the slices on three planes. After that, we redivided the reorganized MRI images into the training set and testing set. After reorganizing 150 images, 120 were used as the training set and 30 as the test set. In the second reconstruction work, we directly used all the slices on the three planes as training and completed the image patching work.

#### 3.1.2. Experimental Environment

Throughout the whole experiment, we built the model under the Pytorch framework and used GPU for network training. The main configuration was a Tesla V100-SXM2 (32 GB) DGX system.

#### 3.1.3. Experimental Configuration

When building a residual network, we considered reducing the network parameters while maximizing the network's efficiency. We compared the situation of the network at different depths (Figures 9 and 10).

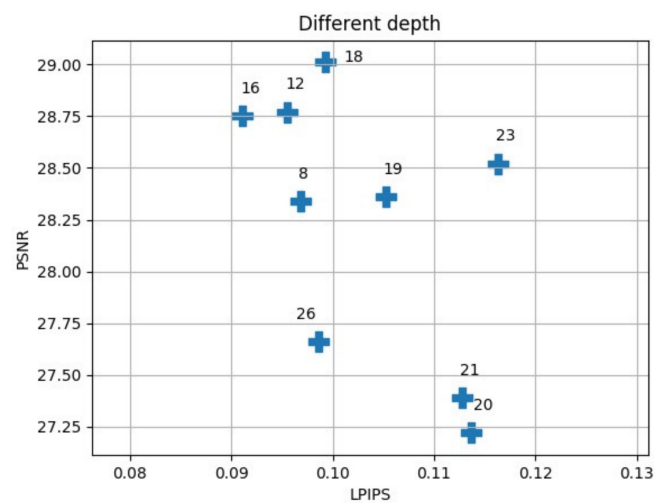


**Figure 9.** Different network depths for super-resolution in this study; 16 blocks performs better than other depths by PSNR and LPIPS. With small network depth, 16 and 12 blocks also perform best. With large network depth, 23 perform best.

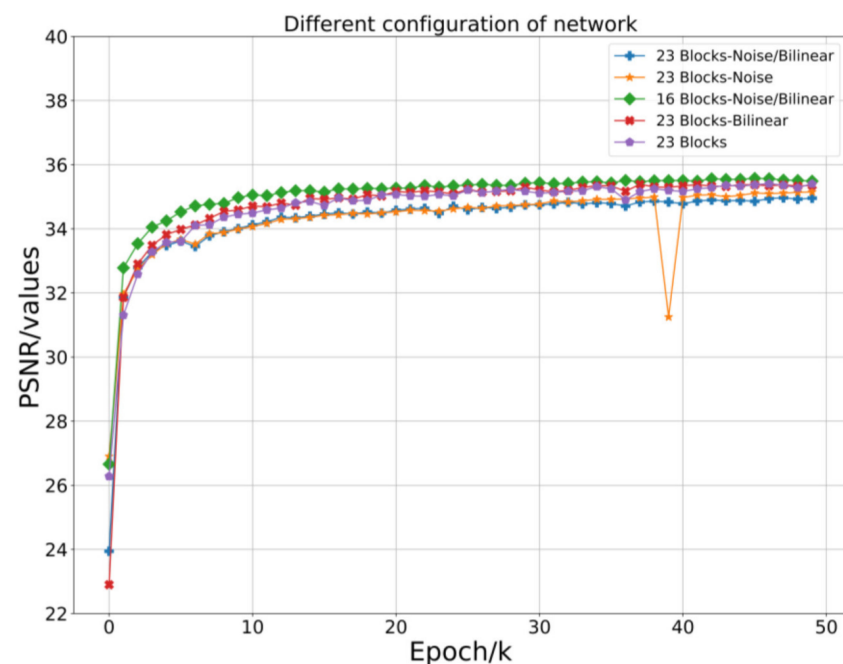


**Figure 10.** Comparison of different depths and structural networks. There is only a noise part compared to the original network, and PSNR is lower. At the same time, the interpolation sampling part is also relatively lower. In both cases, the greater the network depth, the lower the PSNR. The 16-block network with the noise part and interpolation sampling part performs best.

The deeper the network we chose, the better the performance. However, there were also network parameters and calculations that increased. For this reason, we needed to use as little depth as possible while maintaining better efficiency. Therefore, we chose 16 residuals with relatively good performance as the network depth. In the network construction of RFB-ESRGAN, we used 16 residuals in the residual deep network blocks and 8 perceptual field blocks [19,29]. In addition, in nESRGAN, we added an interpolation sampling method in the feature extraction part and the upsampling of the network. At the same time, we added noise to the network to recover detailed information [35]. In Figure 9, 23 is the best performer in the deeper network. Therefore, we compared networks

with smaller and larger depths, and we selected and compared the residual network's performance with 16 and 23 (Table 2). The depth of 16 is superior to 23 in all evaluations.

In the experiment, the batch sizes of the two networks were both suitable for 16 blocks. In the noise part of nESRGAN, the network uses Gaussian noise [28]. We used linear interpolation for feature extraction and upsampling (Figure 6). This setting can avoid the checkerboard effect, while providing more detailed functions.

### 3.2. Comparison

#### 3.2.1. RFB-ESRGAN

We chose RFB-ESRGAN in order to verify its advantages of high-detail information, and compared it with the traditional super-resolution methods in deep learning (Table 1). We found that RFB-ESRGAN performed best in image evaluation indicators and visual quality overall (Figure 11).

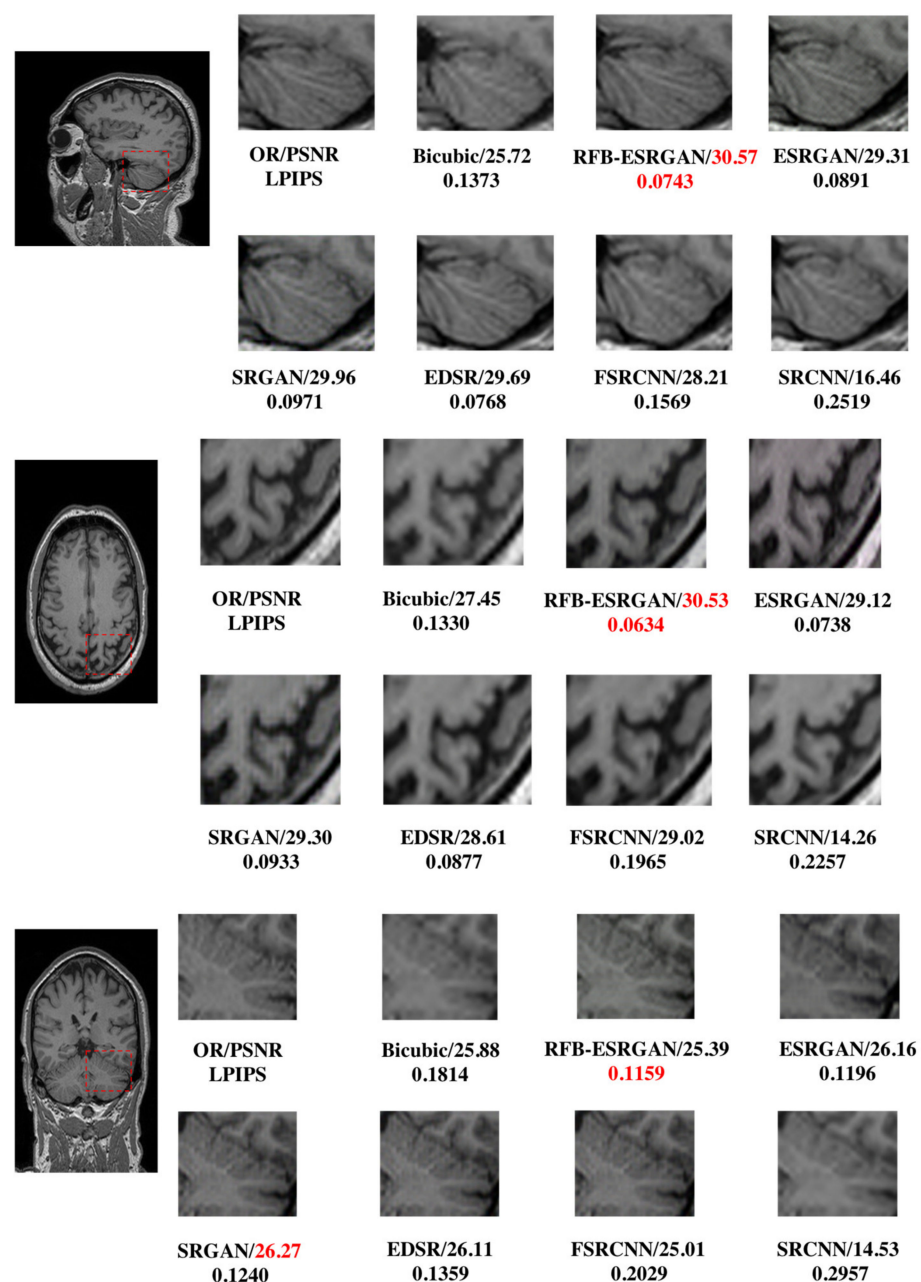


Figure 11. Comparison of SRCNN [36], FSRCNN [27], EDSR [15], SRGAN [17], ESRGAN [18], RFB-ESRGAN [19] in the first reconstruction.

**Table 2.** Comparison of configurations in noise based enhanced super-resolution generated adversarial neural networks (nESRGAN). Red font indicates best performance, blue font indicates second best performance (mean  $\pm$  standard deviation).

Plane/Network	Evaluation	Depth of Residual in Residual Dense Block			Configuration		Original
		23 Blocks Noise/Bilinear	16 Blocks Noise/Bilinear	23 Blocks Noise	23 Blocks Bilinear	23 Blocks	
sagittal	PSNR $\uparrow$	26.36 $\pm$ 1.01	29.63 $\pm$ 0.83	29.58 $\pm$ 1.09	29.83 $\pm$ 1.08	29.28 $\pm$ 1.38	
	SSIM $\uparrow$	0.9289 $\pm$ 0.0130	0.9478 $\pm$ 0.0070	0.9441 $\pm$ 0.0052	0.9450 $\pm$ 0.0056	0.9452 $\pm$ 0.0064	
	LPIPS $\downarrow$	0.1255 $\pm$ 0.0138	0.0955 $\pm$ 0.0124	0.1034 $\pm$ 0.0083	0.1063 $\pm$ 0.0077	0.1116 $\pm$ 0.0080	
coronal	PSNR $\uparrow$	29.42 $\pm$ 1.84	32.12 $\pm$ 1.23	33.36 $\pm$ 1.37	32.17 $\pm$ 1.34	33.18 $\pm$ 1.45	
	SSIM $\uparrow$	0.9353 $\pm$ 0.0033	0.9728 $\pm$ 0.0025	0.9510 $\pm$ 0.0056	0.9584 $\pm$ 0.0018	0.9596 $\pm$ 0.0020	
	LPIPS $\downarrow$	0.0714 $\pm$ 0.0054	0.0586 $\pm$ 0.0056	0.0582 $\pm$ 0.0047	0.0543 $\pm$ 0.0044	0.0533 $\pm$ 0.0048	
transverse	PSNR $\uparrow$	29.16 $\pm$ 0.69	31.33 $\pm$ 0.34	31.32 $\pm$ 0.46	31.04 $\pm$ 0.51	31.17 $\pm$ 0.70	
	SSIM $\uparrow$	0.9222 $\pm$ 0.0016	0.9626 $\pm$ 0.0018	0.9406 $\pm$ 0.0020	0.9435 $\pm$ 0.0018	0.9438 $\pm$ 0.0024	
	LPIPS $\downarrow$	0.0896 $\pm$ 0.0055	0.0731 $\pm$ 0.0040	0.0799 $\pm$ 0.0040	0.0802 $\pm$ 0.0039	0.0877 $\pm$ 0.0052	

### 3.2.2. nESRGAN

In the second reconstruction, considering that we hoped for better performance in the image quality evaluation, we tried to compare the situation after the second reconstruction under different configurations. We separately set the noise and interpolation sampling part, no noise and interpolation sampling part, only the noise part, and only the interpolation sampling part. We considered whether the difference in network depth would affect image reconstruction quality; we also set two depth networks: 16 and 23. We compared them (Table 2) and found that the noise and interpolation sampling part with a depth of 16 performed best. The PSNR comparison chart is shown in Figure 7. For this reason, we selected nESRGAN with a depth of 16 as the second reconstruction network.

## 4. Results

### 4.1. First Super-Resolution Reconstruction

We tested the slices of three planes in the first super-resolution process, and RFB-ESRGAN was superior to other super-resolution methods according to the image evaluation indicators (PSNR, SSIM, LPIPS). Moreover, in terms of detail, RFB-ESRGAN had more detailed features and the best performance in the three planes. The results are shown in Figure 11.

### 4.2. MRI Reconstruction Comparison

After using RFB-ESRGAN for the first reconstruction, we performed the second MRI reconstruction. The recombined MRI image was very noisy and had missing values. Our previous work involved repairing images according to the principle of linear interpolation, using effective pixel value interpolation instead of null values to obtain a new high-resolution MRI image. Nevertheless, our method still has a small amount of noise, and the visual effect is average [37]. Therefore, we compared our proposed nESRGAN with the previous work. After reconstruction, we tested three slices under three planes. As shown in Figure 12, the performance of nESRGAN was far better than our previous work [38]. At the same time, we also compared nESRGAN with advanced super-resolution methods. The MRI image reconstructed by SRCNN had a different brightness between adjacent slices and insufficient detail information. EDSR recovered some detailed information, but there was still noise. Overall, nESRGAN performs better than other methods in visual quality and image evaluation (Figure 12). Based on nESRGAN, we reconstructed the image after the first rebuilding. We realized super-resolution reconstruction of MRI images on the two-dimensional level through the two networks' reconstruction work, successfully replacing the three-dimensional convolutional neural network.

### 4.3. Comparison of 2D and 3D

Three-dimensional reconstruction of MRI images can usually be carried out with a three-dimensional convolutional neural network [22–24]. We also compared traditional 3D MRI super-resolution reconstruction methods [22,23] (Table 3). Compared with 3DSRCNN and 3DSRGAN, our approach maintains advantages in image evaluation and detail comparison (Figure 13).

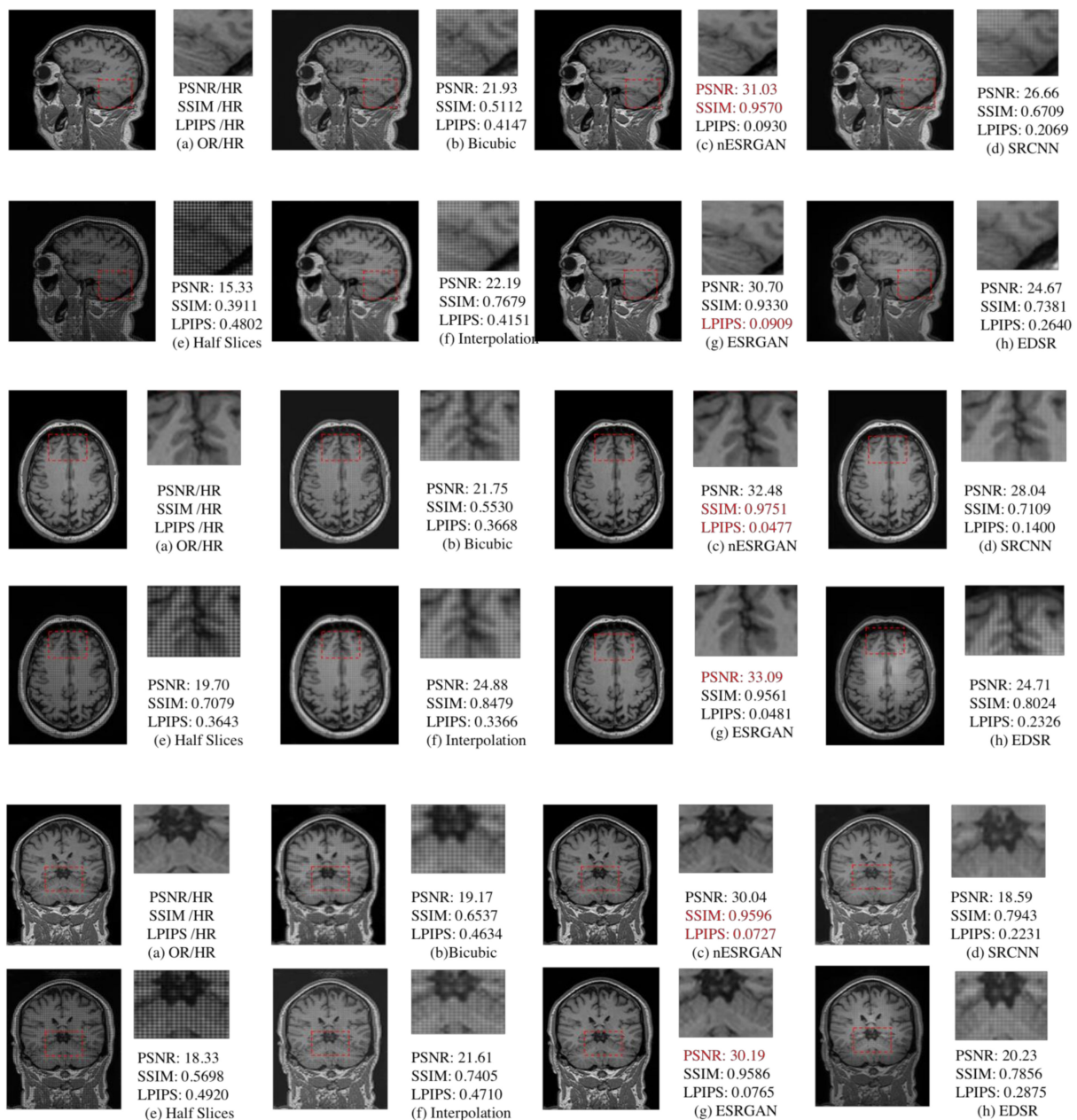


**Figure 12.** Comparison of bicubic, interpolation [38], advanced methods, and nESRGAN. Among them, (a) is the original high-resolution MRI slice, (e) is the slice from reconstructed MRI in the first reconstruction. (b,f) are new slices after interpolation repair. Besides, (d,g,h) are advanced super-resolution methods in deep learning. (c) is our proposed method nESRGAN (nose-based enhanced super-resolution generative adversarial network). (b,d,f,h) still exists a few noises and grid lines which missing value lead. (c,g) perform better than others. The performance of visual quality between (c) and (d) is similar. Furthermore, (c) performs better than (d) in the image quality evaluation.

**Table 3.** Comparison of 2D and 3D methods (mean  $\pm$  standard deviation). Red font indicates best performance; blue font indicates second best performance. Our proposed method performs better than 3D methods.

Plane/Network	Evaluation	Bicubic	3DSRCNN	3DSRGAN	Ours
Sagittal	PSNR $\uparrow$	25.77 $\pm$ 1.32	19.93 $\pm$ 0.9728	23.74 $\pm$ 1.13	30.28 $\pm$ 0.59
	SSIM $\uparrow$	0.8170 $\pm$ 0.0191	0.7240 $\pm$ 0.0346	0.7288 $\pm$ 0.0145	0.9497 $\pm$ 0.0020
	LPIPS $\downarrow$	0.1321 $\pm$ 0.0103	0.3288 $\pm$ 0.0150	0.2236 $\pm$ 0.0102	0.0806 $\pm$ 0.0039
Coronal	PSNR $\uparrow$	19.44 $\pm$ 2.12	24.02 $\pm$ 0.72	24.74 $\pm$ 1.34	34.25 $\pm$ 1.34
	SSIM $\uparrow$	0.6318 $\pm$ 0.0315	0.8838 $\pm$ 0.0183	0.6422 $\pm$ 0.0287	0.9710 $\pm$ 0.0022
	LPIPS $\downarrow$	0.1550 $\pm$ 0.0265	0.2300 $\pm$ 0.0127	0.1723 $\pm$ 0.0149	0.0498 $\pm$ 0.0059
Axial	PSNR $\uparrow$	23.71 $\pm$ 1.69	25.08 $\pm$ 1.73	27.43 $\pm$ 1.84	30.93 $\pm$ 0.90
	SSIM $\uparrow$	0.6901 $\pm$ 0.0299	0.8634 $\pm$ 0.0642	0.7065 $\pm$ 0.0549	0.9596 $\pm$ 0.0053
	LPIPS $\downarrow$	0.1236 $\pm$ 0.0233	0.2471 $\pm$ 0.0234	0.1486 $\pm$ 0.0272	0.0731 $\pm$ 0.0121

## 5. Discussion

The proposed method employs a two-step 2D super-resolution model to reconstruct 3D MRI images in multiple steps. Figure 2 shows the main idea of restructuring after super-resolution. The method we propose in Figure 4 is to improve the resolution based on computational cost. In the super-resolution method of supervised learning, the paired LR-HR data are prepared for research. Brain MRI images contain all kinds of complex and valuable information. Good pairing of MRI data means that it is necessary to recover as much high-frequency information as possible within limited conditions (time, cost of computing). The RFB-ESRGAN we used (Figure 5) is better than other reconstruction methods in acquiring image detail features (Figure 11). It can be seen from Table 1 that RFB-ESRGAN is basically better than all methods in various image evaluation indicators (PSNR, SSIM, LPIPS). In combination with Figure 7, RFB-ESRGAN also achieves an excellent visual effect without artifacts and local blur. The work of traditional super-resolution reconstruction includes the process of image degradation. Based on this condition, our research adopted slice processing in the initial preparation. Under the condition of  $2\times$  mapping combined with the three-dimensional MRI features, we need to treat the input as an image with only half the volume, and the corresponding slices are halved. For this reason, we adopted MRI to separate the pieces. Using RFB-ESRGAN to improve the resolution of half the data (Figure 2), the reconstructed high-resolution slices are reconstituted with MRI (Figure 1), and half of the practical pixel values are missing.

Based on the reconstructed image, our first job is to improve the image resolution while recovering the missing details as much as possible. The last stage in Figure 2 shows the reconstructed image. Traditional interpolation repair generally uses the effective surrounding image pixels to generate the gray value of unknown pixels. However, we tried interpolation in our previous work and the effect was not apparent. As seen in Figure 12, the interpolation method only improves a small part of image. To this end, we need to use super-resolution again for image restoration and resolution enhancement. In the second stage of preparation, we analyzed the role of noise in countering the neural networks. Adding a little noise to the network does not affect the overall amount of calculation and gives the image a little detail. We verified the effectiveness of noise, as shown in Table 2. To avoid the checkerboard effect, we found that interpolation sampling can solve the problem. Our goal is to reduce the computational cost as much as possible and having fewer network parameters can help with this.



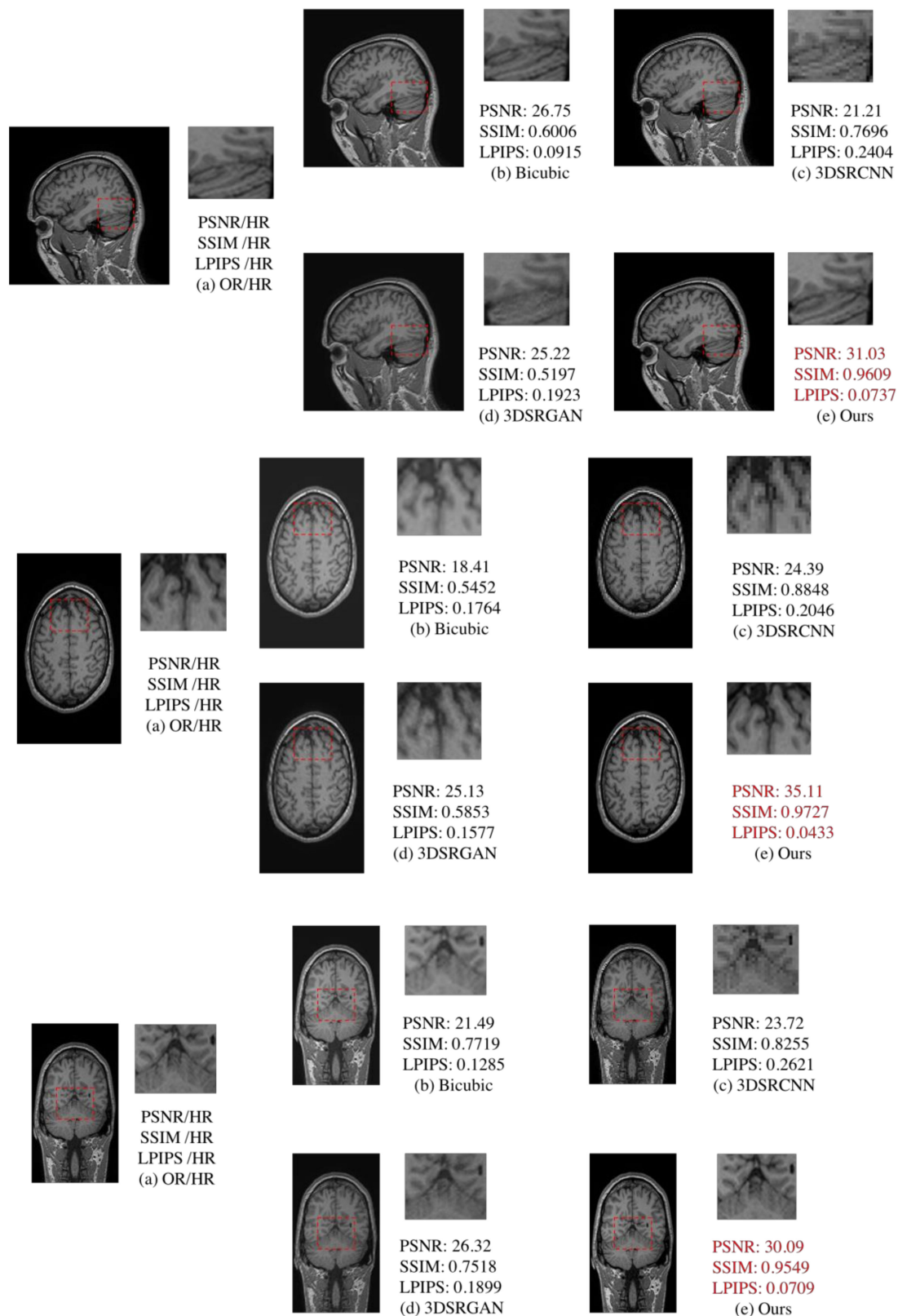


**Figure 13.** Comparison of 3DSRCNN [21], 3DSRGAN [22], bicubic, and proposed method. (a) is the original high-resolution MRI slice. (b) is new slice after interpolation of bicubic. (c,d) are 3D super-resolution methods in deep learning. From this comparison, (e) is our proposed method which includes two super resolution reconstruction steps (RFB-ESRGAN and nESRGAN). (e) performs better than (c,d) in the scope of high-frequency information and visual quality. Besides, (e) also get better performance in the image quality evaluation.

For this reason, we also discussed the depth of the two networks. From Figure 4, it can be seen that extending the depth can improve the image efficiency. However, it can be seen from Table 2 that depth enhancement also affects the image reconstruction quality. Simultaneously, we are considering that the depth of the network is minimized to reduce the amount of calculation, so we chose 16 as the depth of the residual in the residual depth network. As shown in Figure 12, the MRI image reconstructed by nESRGAN is indeed superior in visual and image evaluation compared to the other methods. The addition of noise can restore a small amount of detail. Using nESRGAN, the reconstructed image can be reconstructed with super-resolution again. We use the MRI slice as a degraded image in the data preparation stage and add a downsampling module to the network for feature extraction. The reconstructed MRI slice is directly reconstructed for the second time, and finally the super-resolution reconstruction of 3DMRI is realized.

As shown in Table 3, the method we have proposed in the research is superior to some 3D convolutional neural networks in all aspects. The study shows that it is feasible to reconstruct images twice through super-resolution. Reducing the time cost and computational complexity can help medical staff improve diagnosis and treatment efficiency within a limited time.

## 6. Conclusions

In our experiments, we combined two deep adversarial neural networks to perform the 3D reconstruction of MRI images. We used RFB-ESRGAN based on perceptual information to obtain images with high resolution and a high level of detailed features. After reconstructing the MRI slices, we reorganized the three-latitude high-resolution slices into a three-dimensional MRI image. Then we performed the traversal slice operation again and completed a second reconstruction through the proposed nESRGAN. Finally, we rebuilt the reconstructed new MRI slice for the second time, and finally achieved high-resolution images. Our method is better than traditional 3D super-resolution reconstruction technology in terms of visual effects and image evaluation. In conclusion, the approach we propose successfully achieved 3D reconstruction of MRI images in a 2D field. The reconstructed new images have specific significance in medical diagnosis. Our proposed method only realizes the reconstruction of MRI under the condition of limited zoom factor. In the future, we will try to reconstruct with any size scaling factor, and we also would like to reconstruct MRI based on unsupervised learning.

**Author Contributions:** Conceptualization, H.Z.; methodology, H.Z.; software, H.Z.; validation, H.Z.; formal analysis, S.Y.; investigation, S.Y. and Y.S.; resources, H.Z.; data curation, H.Z.; writing—original draft preparation, H.Z.; writing—review and editing, S.Y.; visualization, S.Y.; supervision, S.Y. and Y.S.; project administration, H.Z.; funding acquisition, S.Y.; All authors have read and agreed to the published version of the manuscript.

**Funding:** This research received no external funding.

**Institutional Review Board Statement:** Not applicable.

**Informed Consent Statement:** Not applicable.

**Data Availability Statement:** Data was obtained from Brain Development and are available <https://brain-development.org/ixi-dataset> (accessed on 20 August 2020) with the permission of CC BY-SA 3.0 license.

**Acknowledgments:** This work was supported by the IXI Dataset, <https://brain-development.org/ixi-dataset/> (accessed on 20 August 2020). This work was also supported by JSPS KAKENHI, grant numbers 17K00312, 19K22763, and 20H00267.

**Conflicts of Interest:** The authors declare no conflict of interest.

## References

1. Duyn, J.H. The future of ultra-high field MRI and fMRI for study of the human brain. *NeuroImage* **2012**, *62*, 1241–1248. [[CrossRef](#)] [[PubMed](#)]
2. Pruessner, J.; Li, L.; Serles, W.; Pruessner, M.; Collins, D.; Kabani, N.; Lupien, S.; Evans, A. Volumetry of Hippocampus and Amygdala with High-resolution MRI and Three-dimensional Analysis Software: Minimizing the Discrepancies between Laboratories. *Cereb. Cortex* **2000**, *10*, 433–442. [[CrossRef](#)] [[PubMed](#)]
3. Soher, B.J.; Dale, B.M.; Merkle, E.M. A Review of MR Physics: 3T versus 1.5T. *Magn. Reson. Imaging Clin. N. Am.* **2006**, *15*, 277–290. [[CrossRef](#)] [[PubMed](#)]
4. Willinek, W.A.; Schild, H.H. Clinical advantages of 3.0T MRI over 1.5T. *Eur. J. Radiol.* **2008**, *65*, 2–14. [[CrossRef](#)] [[PubMed](#)]
5. Greenspan, H.; Oz, G.; Kiryati, N.; Peled, S. MRI inter-slice reconstruction using super-resolution. *Magn. Reson. Imaging* **2002**, *20*, 437–446. [[CrossRef](#)]
6. Elad, M.; Feuer, A. Super-resolution reconstruction of image sequences. *IEEE Trans. Pattern Anal. Mach. Intell.* **1999**, *21*, 817–834. [[CrossRef](#)]
7. Plenge, E.; Poot, D.H.; Bernsen, M.; Kotek, G.; Houston, G.; Wielopolski, P.; van der Weerd, L.; Niessen, W.J.; Meijering, E. February. Super-resolution reconstruction in MRI: Better images faster? In *Medical Imaging 2012: Image Processing*; International Society for Optics and Photonics: San Diego, CA, USA, 2012; Volume 8314, p. 83143V.
8. Plenge, E.; Poot, D.H.J.; Bernsen, M.; Kotek, G.; Houston, G.; Wielopolski, P.; Van Der Weerd, L.; Niessen, W.J.; Meijering, E. Super-resolution methods in MRI: Can they improve the trade-off between resolution, signal-to-noise ratio, and acquisition time? *Magn. Reson. Med.* **2012**, *68*, 1983–1993. [[CrossRef](#)] [[PubMed](#)]
9. Shi, F.; Cheng, J.; Wang, L.; Yap, P.-T.; Shen, D. LRTV: MR Image Super-Resolution with Low-Rank and Total Variation Regularizations. *IEEE Trans. Med Imaging* **2015**, *34*, 2459–2466. [[CrossRef](#)] [[PubMed](#)]
10. Yang, W.; Zhang, X.; Tian, Y.; Wang, W.; Xue, J.-H.; Liao, Q. Deep Learning for Single Image Super-Resolution: A Brief Review. *IEEE Trans. Multimed.* **2019**, *21*, 3106–3121. [[CrossRef](#)]
11. Glasner, D.; Bagon, S.; Irani, M. Super-resolution from a single image. In Proceedings of the 2009 IEEE 12th International Conference on Computer Vision, Kyoto, Japan, 29 September–2 October 2009; pp. 349–356.
12. Protter, M.; Elad, M.; Takeda, H.; Milanfar, P. Generalizing the Nonlocal-Means to Super-Resolution Reconstruction. *IEEE Trans. Image Process.* **2009**, *18*, 36–51. [[CrossRef](#)] [[PubMed](#)]
13. Wang, Z.; Chen, J.; Hoi, S.C.H. Deep learning for image super-resolution: A survey. *IEEE Trans. Pattern Anal. Mach. Intell.* **2020**. [[CrossRef](#)] [[PubMed](#)]
14. He, K.; Zhang, X.; Ren, S.; Sun, J. Deep Residual Learning for Image Recognition. In Proceedings of the 2016 IEEE Conference on Computer Vision and Pattern Recognition (CVPR), Las Vegas, NV, USA, 27–30 June 2016; pp. 770–778.
15. Lim, B.; Son, S.; Kim, H.; Nah, S.; Lee, K.M. Enhanced deep residual networks for single image super-resolution. In Proceedings of the IEEE Conference on Computer Vision and Pattern Recognition Workshops, Honolulu, HI, USA, 21–26 July 2017; pp. 136–144.
16. Tong, T.; Li, G.; Liu, X.; Gao, Q. Image super-resolution using dense skip connections. In Proceedings of the IEEE International Conference on Computer Vision, Venice, Italy, 22–29 October 2017; pp. 4799–4807.
17. Ledig, C.; Theis, L.; Huszar, F.; Caballero, J.; Cunningham, A.; Acosta, A.; Aitken, A.; Tejani, A.; Totz, J.; Wang, Z.; et al. Photo-Realistic Single Image Super-Resolution Using a Generative Adversarial Network. In Proceedings of the 2017 IEEE Conference on Computer Vision and Pattern Recognition (CVPR), Honolulu, HI, USA, 21–26 July 2017; pp. 5892–5900.
18. Wang, X.; Yu, K.; Wu, S.; Gu, J.; Liu, Y.; Dong, C.; Qiao, Y.; Loy, C.C. Esrgan: Enhanced super-resolution generative adversarial networks. In Proceedings of the European Conference on Computer Vision (ECCV) Workshops, Munich, Germany, 8–14 September 2018.
19. Shang, T.; Dai, Q.; Zhu, S.; Yang, T.; Guo, Y. Perceptual extreme super-resolution network with receptive field block. In Proceedings of the IEEE/CVF Conference on Computer Vision and Pattern Recognition Workshops, Virtual, 14–19 June 2020; pp. 440–441.
20. Goodfellow, I.J.; Pouget-Abadie, J.; Mirza, M.; Xu, B.; Warde-Farley, D.; Ozair, S.; Courville, A.; Bengio, Y. Generative adversarial networks. *arXiv* **2014**, arXiv:1406.2661.
21. Odena, A.; Dumoulin, V.; Olah, C. Deconvolution and Checkerboard Artifacts. *Distill* **2016**, *1*, e3. [[CrossRef](#)]
22. Wang, Y.; Teng, Q.; He, X.; Feng, J.; Zhang, T. CT-image of rock samples super resolution using 3D convolutional neural network. *Comput. Geosci.* **2019**, *133*, 104314. [[CrossRef](#)]
23. Sánchez, I.; Vilaplana, V. Brain MRI super-resolution using 3D generative adversarial networks. *arXiv* **2018**, arXiv:1812.11440.
24. Chen, Y.; Xie, Y.; Zhou, Z.; Shi, F.; Christodoulou, A.G.; Li, D. Brain MRI super resolution using 3D deep densely connected neural networks. In Proceedings of the 2018 IEEE 15th International Symposium on Biomedical Imaging (ISBI 2018), Washington, DC, USA, 4–7 April 2018; pp. 739–742.
25. Srinivasan, K.; Ankur, A.; Sharma, A. Super-resolution of magnetic resonance images using deep convolutional neural networks. In Proceedings of the 2017 IEEE International Conference on Consumer Electronics-Taiwan (ICCE-TW), Taipei, Taiwan, 12–14 June 2017; pp. 41–42.
26. Lyu, Q.; Chenyu, Y.; Hongming, S.; Ge, W. Super-resolution MRI through deep learning. *arXiv* **2018**, arXiv:1810.06776.
27. Dong, C.; Loy, C.C.; Tang, X. Accelerating the super-resolution convolutional neural network. In *European Conference on Computer Vision, Proceedings of the 14th European Conference, Amsterdam, The Netherlands, 11–14 October 2016*; Springer: Cham, Switzerland, 2016; pp. 391–407.

28. Karras, T.; Samuli, L.; Timo, A. A style-based generator architecture for generative adversarial networks. In Proceedings of the IEEE/CVF Conference on Computer Vision and Pattern Recognition, Long Beach, CA, USA, 16–20 June 2019; pp. 4401–4410.
29. Liu, S.; Huang, D. Receptive field block net for accurate and fast object detection. In Proceedings of the European Conference on Computer Vision (ECCV), Munich, Germany, 8–14 September 2018; pp. 385–400.
30. Jolicœur-Martineau, A. The relativistic discriminator: A key element missing from standard GAN. *arXiv* **2018**, arXiv:1807.00734.
31. Simonyan, K.; Zisserman, A. Very deep convolutional networks for large-scale image recognition. *arXiv* **2014**, arXiv:1409.1556.
32. Ioffe, S.; Szegedy, C. Batch normalization: Accelerating deep network training by reducing internal covariate shift. In Proceedings of the International Conference on Machine Learning, Lille, France, 6–11 July 2015; pp. 448–456.
33. Horé, A.; Ziou, D. Image quality metrics: PSNR vs. SSIM. In Proceedings of the 20th International Conference on Pattern Recognition, Istanbul, Turkey, 23–26 August 2010; pp. 2366–2369.
34. Zhang, R.; Isola, P.; Efros, A.A.; Shechtman, E.; Wang, O. The unreasonable effectiveness of deep features as a perceptual metric. In Proceedings of the IEEE Conference on Computer Vision and Pattern Recognition, Salt Lake City, UT, USA, 18–23 June 2018; pp. 586–595.
35. Rakotonirina, N.C.; Rasoanaivo, A. ESRGAN+: Further improving enhanced super-resolution generative adversarial network. In Proceedings of the ICASSP 2020—International Conference on Acoustics, Speech and Signal Processing (ICASSP), Barcelona, Spain, 4–8 May 2020; pp. 3637–3641.
36. Dong, C.; Loy, C.C.; He, K.; Tang, X. Learning a deep convolutional network for image super-resolution. In *European Conference on Computer Vision, Proceedings of the 13th European Conference, Zurich, Switzerland, 6–12 September 2014*; Springer: Cham, Switzerland, 2014; pp. 184–199.
37. Hongtao, Z.; Shinomiya, Y.; Yoshida, S. 3D Brain MRI Reconstruction based on 2D Super-Resolution Technology. In Proceedings of the 2020 IEEE International Conference on Systems, Man, and Cybernetics (SMC), Toronto, ON, Canada, 11–14 October 2020; pp. 18–23.
38. Hwang, J.W.; Lee, H.S. Adaptive Image Interpolation Based on Local Gradient Features. *IEEE Signal Process. Lett.* **2004**, *11*, 359–362. [[CrossRef](#)]